Helical CT Reconstruction From Sparse-View Data Through Exploiting the 3D Anatomical Structure Sparsity

YONGBO WANG[1,2,3,6]**, GAOFENG CHEN**[1,3,6]**, XI TAO**[1,3]**, ZHAOYING BIAN**[1,3]**, DONG ZENG**[3,4]**,
HABIB ZAIDI[5]**, (Fellow, IEEE), JI HE**[1,3]**, AND JIANHUA MA**[1,3]

[1]School of Biomedical Engineering, Southern Medical University, Guangzhou 510515, China
[2]Key Laboratory of Intelligent Computing in Medical Image, Ministry of Education, Shenyang 110819, China
[3]Guangzhou Key Laboratory of Medical Radiation Imaging and Detection Technology, Southern Medical University, Guangdong 510515, China
[4]College of Automation Science and Engineering, South China University of Technology, Guangzhou 510641, China
[5]Division of Nuclear Medicine and Molecular Imaging, Geneva University Hospital, CH-1211 Geneva, Switzerland
[6]Pazhou Lab, Guangzhou 510330, China

Corresponding author: Jianhua Ma (jhma@smu.edu.cn)

ABSTRACT Sparse-view scanning has great potential for realizing ultra-low-dose computed tomography (CT) examination. However, noise and artifacts in reconstructed images are big obstacles, which must be handled to maintain the diagnosis accuracy. Existing sparse-view CT reconstruction algorithms were usually designed for circular imaging geometry, whereas the helical imaging geometry is commonly adopted in the clinic. In this paper, we show that the sparse-view helical CT (SHCT) images contain not only noise and artifacts but also severe anatomical distortions. These troubles reduce the applicability of existing sparse-view CT reconstruction algorithms. To deal with this problem, we analyzed the three-dimensional (3D) anatomical structure sparsity in SHCT images. Based on the analyses, we proposed a tensor decomposition and anisotropic total variation regularization model (TDATV) for SHCT reconstruction. Specifically, the tensor decomposition works on nonlocal cube groups to exploit the anatomical structure redundancy; the anisotropic total variation works on the whole volume to exploit the structural piecewise-smooth. Finally, an alternating direction method of multipliers is developed to solve the TDATV model. To our knowledge, the paper presents the first work investigating the reconstruction of sparse-view helical CT. The TDATV model was validated through digital phantom, physical phantom, and clinical patient studies. The results reveal that SHCT could serve as a potential solution for reducing HCT radiation dose to ultra-low level by using the proposed TDATV model.

INDEX TERMS Helical CT, sparse-view, tensor, total variation, iterative reconstruction.

I. INTRODUCTION

Excessive radiation in X-ray CT can cause potential radiation hazard to the patient, raising concerns linked to the increase in cancer risk incidence [1]. Currently, various low-dose CT (LDCT) imaging techniques have been explored including low-mAs [2], [3], sparse-view [4], [5], limited-view [6], and region-of-interest scanning [7]. Among these, the low-mAs technique has been successfully used in commercial CT systems [8]. However, when the mAs is reduced to

ultra-low-dose levels, e.g., tube currents of 10 to 20 mA and exposure time of 0.5 seconds per rotation, photon starvation and electronic noise can pose big challenges to image reconstruction [9]–[11].

Sparse-view CT (SCT) is one of the most promising alternative strategies for ultra-low-dose scanning by reducing the number of projections and maintaining the mAs of each projection at normal levels [5]. SCT can reduce the radiation dose while avoiding photon starvation and reducing the influence of the electronic noise [12]. Many methods have been developed to yield high-quality SCT images [13]. However, these SCT methods are usually performed with

The associate editor coordinating the review of this manuscript and approving it for publication was Vishal Srivastava.
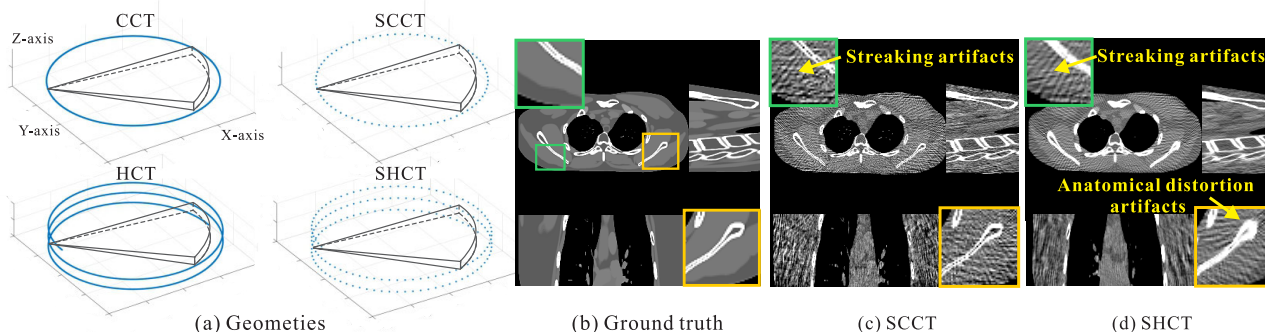
FIGURE 1. (a) Geometries of circular-cone-beam CT (CCT), sparse-view circular-cone-beam CT (SCCT), helical CT (HCT), and sparse-view helical CT (SHCT). The patient table moves in the Z-axis direction; (b) The XCAT digital phantom is used to analyze the artifacts of SHCT reconstruction; (c) The image reconstructed by the FDK algorithm from the 144-view projections with SCCT imaging geometry; (d) The image reconstructed by the WFBP algorithm from 144-view projections with SHCT imaging geometry.

circular fan- or cone-beam geometries that are different from the commonly used helical CT (HCT) in clinic. In general, HCT scans of large organs or the whole human body have higher radiation dose accumulation to patients because of the requirement of collecting multiple rotations of projection data and each rotation requires exposure of hundreds or even more than one thousand projections [14], [15]. Thus, the motivation of this work is to study the sparse-view helical CT (SHCT) reconstruction to reduce the radiation dose to ultra-low level while ensuring the image quality.

Fig. 1 (a) shows the different scanning geometries, including circular-cone-beam CT (CCT), sparse-view circular-cone-beam CT (SCCT), helical CT (HCT), and sparse-view helical CT (SHCT). Modern commercial HCT systems can exactly reconstruct the scanned object because helical scan geometries satisfy Tuy's condition [16], [17]. However, as the number of projections along the helical scan orbit decreases, the reconstruction of the SHCT degenerates into an ill-posed inverse problem. Thus, the classic reconstruction algorithms of HCT are no longer suitable for SHCT reconstruction [17], [18]. Fig. 1 (d) shows the SHCT results of the XCAT phantom reconstructed by the weighted filtered backprojection (WFBP) algorithm, which is implemented by the FreeCT software package [18], [19]. Compared with SCCT, the artifacts of SHCT reconstruction contain not only severe streaking artifacts but also complex anatomical distortion artifacts, which can shadow real anatomical structures, as shown in Figs. 1 (b)-(d).

To address these problems, in this study, we first analyze the SHCT scanning geometry and reconstruction in detail. Based on the analyses, a tensor decomposition and anisotropic total variation regularization model (TDATV) is proposed for SHCT reconstruction. The contributions of this work can be summarized as follows:

- To the best of our knowledge, this is the first work investigating the sparse-view helical CT (SHCT) reconstruction and reducing its radiation dose to ultra-low level;
- We propose a TDATV regularization model by exploiting the 3D anatomical structure sparsity of SHCT

images. Specifically, the tensor decomposition works on nonlocal cube groups to exploit the anatomical structure redundancy and the anisotropic total variation works on the whole volume to exploit the structural piecewise-smooth;
- We validated the potential of the proposed TDATV model with various SHCT data, including digital phantom, physical phantom, and clinical patient data. The results reveal that SHCT could serve as a potential solution for reducing HCT radiation dose to ultra-low level by using the proposed TDATV model.

II. RELATED WORK

In this section, we briefly review previous literature related to this work: the HCT reconstruction algorithms and the SCT reconstruction algorithms.

A. HELICAL CT RECONSTRUCTION ALGORITHMS

For decades, the filtered back-projection (FBP) algorithm has been the dominant reconstruction method in commercial HCT scanners for its simplicity and low computation time [17], [18], [20]. Another type of reconstruction technique, iterative reconstruction (IR), was put away from the clinical application because of its high computation burden. But the situation is changing. The rapid development of high-performance computing chips such as graphics processing units (GPUs) brings the opportunity to IR algorithms. During the past years, several commercial IR techniques (e.g. ASIR of GE Healthcare, SAFIRE of Siemens Healthcare) have been released by the vendors [8]. Moreover, several studies suggested that IR can provide the image with better diagnostic performance against the conventional FBP algorithm at lower radiation dose [8], [11]. The effectiveness of IR depends on two major concerns in practice: the proper prior assumptions and optimization algorithms. Therefore, various advanced prior assumptions have been proposed to meet different low-dose scanning tasks including limited-view [6], sparse-view [12], low-mAs [21], etc. On the other hand, many efficient methods have been extended to optimize the cost function of IR in CT imaging, such as linearized

augmented Lagrangian method (LALM) [22], alternating direction method of multipliers (ADMM) [23], etc.

B. SPARSE-VIEW CT RECONSTRUCTION ALGORITHMS

In SCT reconstruction, the sparsity-regularized methods from compressive sensing (CS) theory have achieved acceptable results in SCT reconstruction, e.g., TV-based regularization [4], [5]. However, the isotropic edge characteristics of traditional TV neglect the slight pixel value flux leading to over-smoothing or patchy artifacts in the sparse-view CT reconstruction. The nonlocal means (NLM) type methods are developed to take advantage of the anatomical structure redundancy of CT images. NLM restores the image by replacing the intensity of each pixel with a weighted average of its neighbors according to similarity [24], [25]. However, most NLM-based methods usually employ a weighted average operation directly on all neighbor pixels with a fixed filtering parameter during the filtering process, ignoring the non-stationary noise characteristics of CT images [26]. The low-rank priors are also explored to constrain the correlation between different image frames, e.g., between multi-energy-bin images in energy-resolved CT and time sequence images in perfusion CT [12], [21]. Recently, the deep neural networks (DNN) also have been incorporated as a regularization term into the IR [27]–[29]. For example, Chen *et al.* presented a learned experts assessment-based reconstruction network (LEARN) for SCT reconstruction, which can be trained by a sparse sinogram and the corresponding full-view images, and the learned regularization terms and balancing parameters are specific to each iteration [29]. Moreover, some studies have proposed a more general reconstruction framework, from sinogram domain to image domain, relying on the fully connected layer or convolutional layer to learn the physical imaging process of CT [30], [31]. Although these SCT reconstruction methods have achieved acceptable results in circular fan- or cone-beam geometries, they are difficult to apply directly to SHCT reconstruction due to the special geometry of SHCT and the more complex artifact and noise distribution. Therefore, in this work, we will present an advanced regularization for the SHCT iterative reconstruction.

III. SPARSE-VIEW HELICAL CT ANALYSIS

A. SHCT GEOMETRY AND IMAGING MODEL

As shown in Fig. 1, taking the patient table as the reference coordinate, the sparse-view helical exposure trajectory $O(n)$ can be described in the 3D Cartesian coordinate system:

$$O(n) = \left(R_F \cos\left(\frac{2\pi N_d}{\bar{N}}n\right), R_F \sin\left(\frac{2\pi N_d}{\bar{N}}n\right), \frac{R_P N_d}{\bar{N}}n \right) \tag{1}$$

where $\bar{N}$ is the number of projections per complete rotation in a full-view HCT scan (e.g., $\bar{N}$ is 2304 in the flying focal spot along axial direction (FFSZ) protocol for the Siemens SOMATOM Definition AS+ scanner), n represents the

sampling point, R_F is the distance from the source to the center of the rotation, R_P is the helical pitch (table feed per rotation), and N_d is the sparse-sampling factor. In particular, $N_d = 1$ denotes the full-view projections. For simplicity, we denote $\bar{N}_s = \bar{N}/N_d$ as the number of projections per complete rotation in an SHCT scan.

The imaging model of SHCT can be approximated as follows:

$$\mathcal{Y} = A\mathcal{X} + \mathcal{N}. \tag{2}$$

Here, $\mathcal{Y} \in \mathbb{R}^{N_u \times N_v \times N_s}$ is the projection data, where N_u is the number of detector rows, N_v is the number of detector channels, and N_s is the number of projections; A represents a projection operator; $\mathcal{X} \in \mathbb{R}^{N_i \times N_j \times N_k}$ is the reconstructed image, where N_i, N_j and N_k denote the number of voxels along the three axis; $\mathcal{N} \in \mathbb{R}^{N_u \times N_v \times N_s}$ is the noise term. Consequently, the iterative reconstruction model for SHCT can be formulated as follows:

$$\min x \mathcal{R}(\mathcal{X}), \quad s.t., \quad \frac{1}{2}\|A\mathcal{X} - \mathcal{Y}\|_{\Sigma^{-1}}^2 \le \varepsilon, \tag{3}$$

where $\mathcal{R}(\mathcal{X})$ is the regularization term associated with the image prior structures. $\Sigma^{-1} = diag\{1/\sigma_i^2\}$ ($1 \le i \le N_u \cdot N_v \cdot N_s$) denotes the weighting diagonal matrix and σ_i^2 is the variance in the ith entry of projection $\mathcal{Y}$. σ_i^2 can be obtained by the mean-variance relationship [2].

B. THE SHCT RECONSTRUCTION ARTIFACTS AND NOISE ANALYSIS

To analyze the artifacts of SHCT reconstruction, we consider a noise-free simulation using the XCAT phantom, i.e., the projection data are not contaminated by any noise. We also simulated noise-free SCCT data for the artifact comparison between SHCT and SCCT. Specifically, the number of projections per complete rotation for both scanning geometries is 144, and they have the same scanning parameters refer to the Siemens SOMATOM Definition AS+ system, except for the pitch factors that are 0 and 0.6 for the SCCT and SHCT, respectively. The simulated SCCT and SHCT data are reconstructed by the FDK and WFBP algorithms, respectively, as shown in Figs. 1 (c) and (d). The insufficient projections of SHCT not only cause serious streaking artifacts but also introduce complex anatomical distortion artifacts, which can shadow real anatomical structures. The main cause of the anatomical distortion artifacts is that in the helical geometry, the moving patient table exacerbates the undersampling of the object to be reconstructed. Another reason is that the convention HCT reconstruction algorithms, such as the WFBP algorithm that requires the complete projection view to accurately perform the backprojection interpolation [18], [19], cannot be directly applied to SHCT reconstruction due to the limitation of incomplete data acquisition. To distinguish the artifacts of the SCCT, the SHCT artifacts, including the streaking and anatomical distortion artifacts, are referred to as sparse-view helical artifacts (SHAs).

In real acquisitions, the normal-mAs projection data are still contaminated by measurement noise, e.g., quantum and

electronic noise. Although existing commercial HCT systems do not provide the sparse-view scan protocols, we can simulate SHCT data from the real HCT projection data, i.e., digitally extracting sparse-view data from the full-view normal-dose projection data at equal intervals. In this study, we used the Mayo challenge data for SHCT simulations [32]. Fig. 2 shows the patient images reconstructed by the WFBP algorithm from the 288-view (1/8 dose) and 144-view (1/16 dose) SHCT projections. In addition to artifacts, SHCT images are also contaminated by noise. The reason is that SHCT reconstruction with insufficient projection is more sensitive to projection noise, while normal dose projections contain measurement noise.
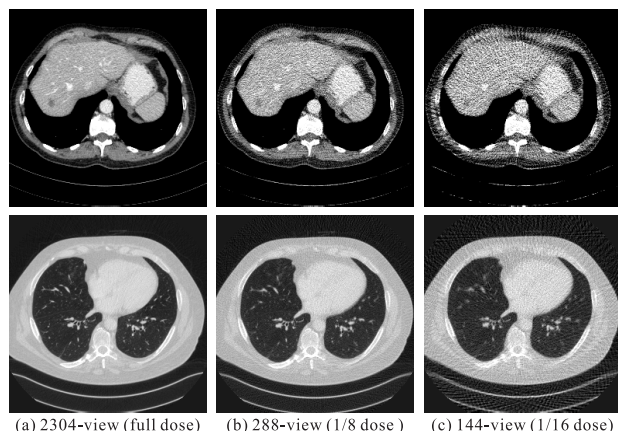

$\mathcal{X} \approx \mathcal{C} \times_1 \mathbf{U}_1 \times_2 \mathbf{U}_2 \times_3 \mathbf{U}_3$

(a) HCT	(b) Core Tensor $\mathcal{C}$	(c) Typical slice of $\mathcal{C}$

FIGURE 3. (a) A HCT image $\mathcal{X} \in \mathbb{R}^{80 \times 80 \times 40}$ and it's Tucker decomposition; (b) Core tensor $\mathcal{C} \in \mathbb{R}^{80 \times 80 \times 40}$ of $\mathcal{X}$ and note that 72.4% of its elements are zeros; (c) Typical slices of $\mathcal{C}$.

(a) 2304-view (full dose)	(b) 288-view (1/8 dose)	(c) 144-view (1/16 dose)

FIGURE 2. (a)-(c) Images reconstructed by the WFBP algorithm from 2304-, 288-, and 144-view projections. The top and bottom images are displayed in the window [−140, 260] and [−1150, 350], respectively.

C. THE 3D ANATOMICAL STRUCTURE SPARSITY FOR SHCT IMAGING

1) ANATOMICAL STRUCTURE REDUNDANCY

In this section, we first analyze the anatomical structure redundancy of the CT images including the structural correlation and self-similarity. Tucker decomposition or CANDECOMP/PARAFAC (CP) low-rank decomposition is capable of characterizing the correlation information of 3D CT images. Fig. 3 shows the schematic diagrams of Tucker decomposition and the non-zeros element distribution of core tensor for the 3D CT image. It can be observed that the core tensor contains a large number of zero elements, indicating that the 3D CT image is low-rank and therefore possesses good correlation property. However, the Tucker and CP decomposition both have their disadvantage, such as the CP decomposition cannot well encode the low-rank property of the tensor subspaces along with its modes, and the Tucker decomposition has not considered the fine-grained sparsity configurations inside this coefficient tensor [33], [34]. Currently, the Kronecker-basis-representation (KBR) -based tensor decomposition have been proposed to address these problems, which encodes both sparsity insights delivered by Tucker and CP decompositions for a general tensor. In particular, KBR-based tensor decomposition has achieved
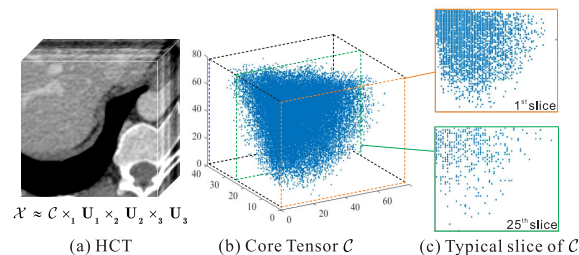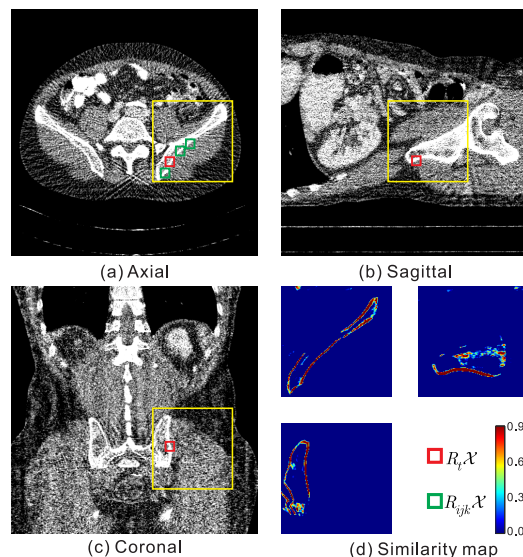

(a) Axial	(b) Sagittal
(c) Coronal	(d) Similarity map

FIGURE 4. Anatomical structure self-similarity analysis of the SHCT image. The yellow boxes is the search window. $R_t \mathcal{X}$ and R_{ijk} represent the target and extracted cubes, respectively.

state-of-the-art performance on the low-mAs perfusion and energy-resolved CT reconstructions [21], [34]. Thus, inspired by these works, the KBR-based tensor decomposition is introduced to characterize the structural correlation of the 3D CT image.

On the other hand, to exploit the structural self-similarity property of the SHCT image, we cropped out region-of-interest (ROIs) in different anatomical regions and computed their similarity maps. The exponent of the negative Euclidean distance was adopted to describe the similarity between the ROIs:

$$\mathcal{S}_{ijk} = \mathbf{exp}\{-\|R_t \mathcal{X} - R_{ijk}\mathcal{X}\|^2\}, \qquad (4)$$

where R denotes a cube extracting operator, $R_t \mathcal{X}$ and R_{ijk} represent the target and extracted cubes, respectively. Fig. 4 shows the similar maps computed with the pelvis anatomical structures in 144-view reconstruction. The similarity maps quantitatively demonstrate pelvis has good structural self-similarity. In general, other anatomical structures also have good structural self-similarity. Therefore, considering the structural correlation and self-similarity, we introduce the KBR-based tensor decomposition to describe the 4-order
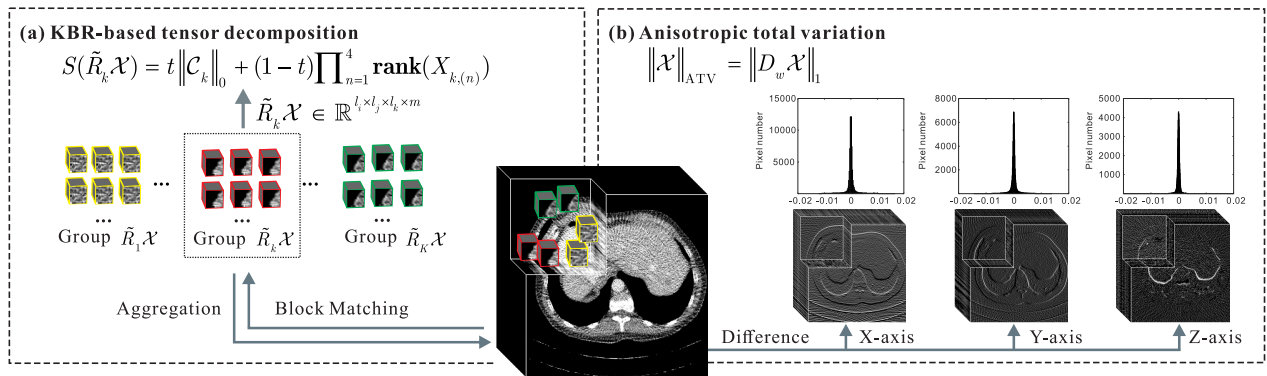
FIGURE 5. The proposed tensor decomposition and anisotropic total variation regularization model (TDATV). (a) Schematic of KBR-based tensor decomposition. The groups $\tilde{R}_k \mathcal{X}$ ($k = 1, 2, \ldots, K$) are obtained through block matching within a large local window and stacked to the corresponding clean temporary tensors. Then, the clean temporary tensors can be estimated by the KBR-based tensor decomposition. By aggregating the clean temporary tensors, restored SHCT images can be obtained; (b) Illustration of the Piecewise-smooth structure of SHCT images along with different modes, wherein the lower row is the gradient maps along with different modes, and the upper row is the frequency of the gradient maps.

low-rank anatomical tensors stacked by the corresponding groups of nonlocal cubes that contain rich anatomical redundancy for SHCT reconstruction, as shown in Fig. 5 (a).

2) PIECEWISE-SMOOTH
The structural piecewise-smooth can associate with the gradient sparsity of the 3D SHCT image. As shown in Fig. 5 (b), most of the difference values between adjacent voxels in three dimensions are nearly equal to zero, which indicates that a large number of piecewise-smooth structures exist in SHCT images. Previous works have established that total variation (TV) is a powerful regularization that can effectively enhance piecewise-smooth structures of CT images to suppress streaking artifacts in SCT reconstructions [4], [35]. Besides, in the 3D SHCT reconstruction, since Z-axial voxel spacing (thickness) is generally not equal to the in-plane voxel spacing, the regularization strength of TV in the axial and in-plane directions is different. Thus, we introduce an anisotropic TV (ATV) regularizer into the KBR-based tensor decomposition framework, which to characterize the structural piecewise-smooth of SHCT images [35].

Finally, considering the 3D anatomical structure sparsity in SHCT imaging, the tensor decomposition and anisotropic total variation regularization model (TDATV) is proposed for SHCT iterative reconstruction in this study.

IV. METHODS
A. TENSOR DECOMPOSITION AND ANISOTROPIC TOTAL VARIATION REGULARIZATION MODEL (TDATV)
As analyzed above, we introduce a KBR-based tensor decomposition to describe the 4-order low-rank tensors stacked by the corresponding groups of nonlocal cubes and adopt an ATV regularization to characterize the structural piecewise-smooth of SHCT images. The proposed TDATV algorithm can be formulated as follows:

$$\min_{\mathcal{X}} \kappa \sum_{k=1}^{K} S(\tilde{R}_k \mathcal{X}) + \beta \|\mathcal{X}\|_{ATV}$$
$$s.t., \frac{1}{2}\|A\mathcal{X} - \mathcal{Y}\|_{\Sigma^{-1}}^2 \leq \varepsilon, \quad (5)$$

Here, $S(\cdot)$ and $\|\cdot\|_{ATV}$ are the KBR and ATV terms, respectively. κ and β are the tradeoff parameters. $\tilde{R}_k \mathcal{X} \doteq [R_{k_1}\mathcal{X}, R_{k_2}\mathcal{X}, \ldots, R_{k_m}\mathcal{X}] \in \mathbb{R}^{l_i \times l_j \times l_k \times m}$ denotes a 4-order tensor formed by a group of image cubes similar to the k-th exemplar cube $\mathcal{X}_k$ (including $\mathcal{X}_k$ itself), R_k denotes an operator extracting the k-th cube $\mathcal{X}_k$ from $\mathcal{X}$, m is the number of the nonlocal similar cubes, and K is the total number of groups [36]. In our experiments, the search window size is $60 \times 60 \times 16$, and the group of nonlocal cubes size is $5 \times 5 \times 5 \times 50$.

1) KBR-BASED TENSOR DECOMPOSITION
In each iteration, the groups $\tilde{R}_k \mathcal{X}$ ($k = 1, 2, \ldots, K$) are first obtained through block matching within a large local window (e.g., $60 \times 60 \times 16$) and stacked separately to the corresponding 4-order tensors, as shown in Fig. 5 (a). The KBR-based decomposition for a tensor $\tilde{R}_k \mathcal{X}$ can be formulated as follows:

$$S(\tilde{R}_k \mathcal{X}) = t\|\mathcal{C}_k\|_0 + (1-t)\prod_{n=1}^{4} \mathbf{rank}\left(\mathbf{X}_{k,(n)}\right), \quad (6)$$

where $\|\cdot\|_0$ denotes the l_0 norm, $\mathcal{C}_k$ denotes the core tensor of $\tilde{R}_k \mathbf{X}$ with the higher order singular value decomposition (HOSVD) [37], $\mathbf{X}_{k,(n)} = \mathbf{unfold}_n(\tilde{R}_k \mathcal{X})$ represents the mode-n unfolding matrix, and $0 < t < 1$ is the penalty parameter controlling the tradeoff between two terms. Moreover, $\|\cdot\|_0$ and $\mathbf{rank}(\cdot)$ can be relaxed by the log-sum form to simplify computation as follows [33]:

$$S^*(\tilde{R}_k \mathcal{X}) = tP(\mathcal{C}_k) + (1-t)\prod_{n=1}^{4} P^*\left(\mathbf{X}_{k,(n)}\right). \quad (7)$$

Here,

$$P(\mathcal{B}) = \sum_{i_1,\ldots,i_N} \left(\log(\|b_{i_1,\ldots,i_N}\| + \epsilon) - (\log(\epsilon))\right)/(-\log(\epsilon)),$$

$$P^*(\mathbf{B}_{(n)}) = \sum_d \left(\log(\sigma_d(\mathbf{B}_{(n)}) + \epsilon)) - (\log(\epsilon))\right)/(-\log(\epsilon)),$$

where $b_{i_1,\ldots,i_N}$ denotes a element of $\mathcal{B}$, $\sigma_d(\mathbf{B}_{(n)})$ defines the dth singular value of $\mathbf{B}_{(n)}$, and ϵ is a small positive number.

2) ANISOTROPIC TOTAL VARIATION

An ATV regularization is incorporated into the KBR-based tensor decomposition framework to fully explore the Piecewise-smooth structure in three directions (X-, Y-, and Z-axis) of SHCT images, as shown in Fig. 5 (b). ATV can be formulated as follows [35]:

$$\|\mathcal{X}\|_{ATV} = \|D_w \mathcal{X}\|_1, \qquad (8)$$

Here, $D_w = [w_1 D_1; w_2 D_2; w_3 D_3]$ is the so-called weighted three-dimensional difference operator. D_1, D_2, D_3 are the first-order difference operators with respect to three different directions of the volume image. $\omega_n (n = 1, 2, 3)$ is the weight along the n-th direction of $\mathcal{X}$ to control its regularization strength. Specifically, $\omega_1 = \omega_2 = 1$ and $\omega_3 = d_{x-y}/d_z$, where d_{x-y} is the in-plane voxel spacing and d_z is the slice thickness.

B. OPTIMIZATION

To efficiently solve the proposed TDATV, we first introduce the auxiliary variables $\mathcal{Z}_k$ $(k = 1, \ldots, K)$ and $\mathcal{T}$:

$$\min_{\mathcal{X}, \{\mathcal{Z}_k\}_{k=1}^K, \mathcal{T}} \kappa \sum_{k=1}^K \left\{ P(\mathcal{C}_k) + \gamma \prod_{n=1}^4 P^* \left(\mathbf{Z}_{k,(n)} \right) \right\}$$
$$+ \beta \|\mathcal{T}\|_1$$
$$s.t., \ \frac{1}{2} \|A\mathcal{X} - \mathcal{Y}\|_{\Sigma^{-1}}^2 \leq \varepsilon,$$
$$\tilde{R}_k \mathcal{X} - \mathcal{Z}_k = 0 \quad (k = 1, \ldots, K),$$
$$\mathcal{T} - D_w \mathcal{X} = 0, \qquad (9)$$

where $\gamma = (1 - t)/t$. $\|\cdot\|_1$ denotes the l_1 norm. This problem has the augmented Lagrangian function as follows:

$$\mathcal{L} \left(\mathcal{X}, \{\mathcal{Z}_k, \mathcal{F}_{\mathcal{Z}_k}\}_{k=1}^K, \mathcal{T}, \mathcal{F}_{\mathcal{T}} \right)$$
$$= \kappa \sum_{k=1}^K \left\{ P(\mathcal{C}_k) \right.$$
$$+ \gamma \prod_{n=1}^4 P^* \left(\mathbf{Z}_{k,(n)} \right) + \frac{\mu}{2\kappa} \|\tilde{R}_k \mathcal{X} - \mathcal{Z}_k + \frac{1}{\mu} \mathcal{F}_{\mathcal{Z}_k}\|_F^2 \right\}$$
$$+ \beta \|\mathcal{T}\|_1 + \frac{\mu}{2} \|D_w \mathcal{X} - \mathcal{T} + \frac{1}{\mu} \mathcal{F}_{\mathcal{T}}\|_F^2 + \frac{1}{2} \|A\mathcal{X} - \mathcal{Y}\|_{\Sigma^{-1}}^2,$$
$$(10)$$

where $\|\cdot\|_F^2$ denotes the Frobenius norm; $\mathcal{F}_{\mathcal{T}}$ and $\mathcal{F}_{\mathcal{Z}_k}$ are the Lagrange multipliers; μ is the positive penalty scalar.

1) UPDATE $\mathcal{X}$

With other parameters fixed, all items related to $\mathcal{X}$ are extracted from Eq. (10):

$$\min_{\mathcal{X}} \frac{1}{2} \|A\mathcal{X} - \mathcal{Y}\|_{\Sigma^{-1}}^2 + \sum_{k=1}^K \frac{\mu}{2} \|\tilde{R}_k \mathcal{X} - \mathcal{Z}_k^{(t)}$$
$$+ \frac{1}{\mu} \mathcal{F}_{\mathcal{Z}_k}^{(t)}\|_F^2 + \frac{\mu}{2} \|D_w \mathcal{X} - \mathcal{T}^{(t)} + \frac{1}{\mu} \mathcal{F}_{\mathcal{T}}^{(t)}\|_F^2, \quad (11)$$

Eq. 11 can be solved by the gradient descent method, and the corresponding solution can be written as follows:

$$\mathcal{X}^{(t+1)} = \mathcal{X}^{(t)} + \eta A^T (A\mathcal{X}^{(t)} - \mathcal{Y}) + \sum_{k=1}^K \mu \tilde{R}_k^* (\tilde{R}_k \mathcal{X}^{(t)}$$
$$- \mathcal{Z}_k^{(t)} + \frac{1}{\mu} \mathcal{F}_{\mathcal{Z}_k}^{(t)}) + \mu D_w^* (D_w \mathcal{X}^{(t)} - \mathcal{T}^{(t)} + \frac{1}{\mu} \mathcal{F}_{\mathcal{T}}^{(t)})$$
$$(12)$$

where $\tilde{R}_k^*$ and D_w^* indicate the adjoint operator of $\tilde{R}_k$ and D_w, respectively, and $\eta \in (0, 2)$ is a relaxation factor [34].

2) UPDATE $\mathcal{Z}_k$

With $\mathcal{Z}_j$ $(j \neq k)$ and other parameters fixed, all items related to $\mathcal{Z}_k$ are extracted from Eq. (10):

$$\min_{\mathcal{Z}_k} \frac{\mu}{2} \|\tilde{R}_k \mathcal{X}^{(t+1)} - \mathcal{Z}_k + \frac{1}{\mu} \mathcal{F}_{\mathcal{Z}_k}^{(t)}\|_F^2 + P(\mathcal{C}_k)$$
$$+ \gamma \prod_{n=1}^4 P^* \left(\mathbf{Z}_{k,(n)} \right). \quad (13)$$

We can solve Eq. (13) under the split-Bregman method, and detail derivation is provided in the supplement.

3) UPDATE $\mathcal{T}$, $\mathcal{F}_{\mathcal{Z}_k}$, AND $\mathcal{F}_{\mathcal{T}}$

With the other parameters fixed, we can update $\mathcal{T}$ by solving the following:

$$\min_{\mathcal{T}} \beta \|\mathcal{T}\|_1 + \frac{\mu}{2} \|D_w \mathcal{X}^{(t+1)} - \mathcal{T} + \mathcal{F}_{\mathcal{T}}^{(t)}\|_F^2. \quad (14)$$

By introducing the soft-thresholding operator:

$$H_\Delta(b) = \begin{cases} b - \Delta, & b > \Delta \\ b + \Delta, & b < \Delta \\ 0, & otherwise, \end{cases} \quad (15)$$

where $b \in \mathbb{R}$ and $\Delta > 0$, then we can update $\mathcal{T}$ as follows:

$$\mathcal{T}^{(t+1)} = H_{\beta/\mu}(D_w \mathcal{X}^{(t+1)} + \mathcal{F}_{\mathcal{T}}^{(t)}). \quad (16)$$

Lagrange multipliers are updated as follows:

$$\mathcal{F}_{\mathcal{Z}_k}^{(t+1)} = \mathcal{F}_{\mathcal{Z}_k}^{(t)} + \mu(\tilde{R}_k \mathcal{X}^{(t+1)} - \mathcal{Z}_k^{(t+1)}), \quad (17)$$
$$\mathcal{F}_{\mathcal{T}}^{(t+1)} = \mathcal{F}_{\mathcal{T}}^{(t)} + \mu(D_w \mathcal{X}^{(t+1)} - \mathcal{T}^{(t+1)}). \quad (18)$$

In summary, the optimization algorithm for the TDATV can be described as algorithm 1. In the implementation, the key parameters (γ, κ, β, and μ) used in the proposed method are manually determined to reach the largest peak signal-to-noise ratio (PSNR) value for phantom data and meet the best feature similarity (FSIM) for patient data [3]. Specifically, $\gamma = 10$, $\kappa = 5 \times 10^5$ and $\mu = 0.01$ in all experiments; β is set as 1×10^5 in the XCAT phantom experiments and is set as 4×10^5 in the CIRS ATOM physical phantom and clinical patients experiments.

Algorithm 1 TDATV for SHCT Reconstruction

Input: $\mathcal{Y}$, Σ^{-1}, γ, κ, β, and other parameters.

  while the stopping criteria are not satisfied **do**

      Update $\mathcal{X}^{(t+1)}$ by Eq. (12);

      Update all $\mathcal{Z}_k^{(t+1)}$ by Eq. (13);

      Update all $\mathcal{F}_{\mathcal{Z}_k}^{(t+1)}$ by Eq. (17);

      Update $\mathcal{T}^{(t+1)}$ by Eq. (16);

      Update $\mathcal{F}_{\mathcal{T}}^{(t+1)}$ by Eq. (18);

  end while

Output: $\mathcal{X}$

C. DATA ACQUISITION

In this work, the XCAT phantom is adopted for the numerical simulation experiment and simulated with the pitch factor of 0.6, and tube voltage of 100 kVp, tube current of 200 mA [38]. The SHCT projection data of the CIRS ATOM physical phantom and clinical patients are simulated from real projection data (acquired on the Siemens SOMATOM Definition AS+ scanner), i.e., digitally extracting the SHCT data from the full-view normal-dose HCT projection data at equal intervals. The patient data are provided and authorized by the Mayo Clinic, which include HCT projection data from 10 different patients who were scanned under the FFSZ and automatic exposure control (AEC) [32]. The selected patient cases in our experiment were acquired with the tube voltage of 100 or 120 kVp and exposure time of 0.5 seconds per rotation. In our experiments, the dimension of the detector array is 736×64 and the size of the detector unit is 1.2858×1.0947 mm^2; the distance from the source to the center of rotation is 595.0 mm and the distance between the source and the detector is 1085.6 mm; the number of projections per complete rotation in the standard scan is 1152-view.

V. EXPERIMENTS AND RESULTS

In our experiments, the WFBP algorithm with a medium-sharpness kernel, provided by the FreeCT software package [19], is selected as the baseline method for comparison. Moreover, the TV [4], nonlocal TV (NLTV) [39], and KBR [33] regularization are applied to the SHCT iterative reconstruction model Eq. (8) as the comparative methods. The experiments are conducted in MATLAB 2016b on a Linux OS with a PC workstation configured with an NVIDIA Tesla P40 GPUs. Moreover, the peak signal-to-noise ratio (PSNR) and feature similarity (FSIM) are chosen for the quantitative analysis [40].

A. PHANTOM STUDY

Fig. 6 shows the results of the XCAT phantom reconstructed by five algorithms from 144-view projections (shown for the central axial, sagittal, and coronal planes). It can be observed that the WFBP result of the 144-view is corrupted by severe noise and SHAs. The TV and NLTV algorithms can suppress the artifacts and noise, while they also cause the reconstructed images to be smoothed, as indicated by the red arrows.
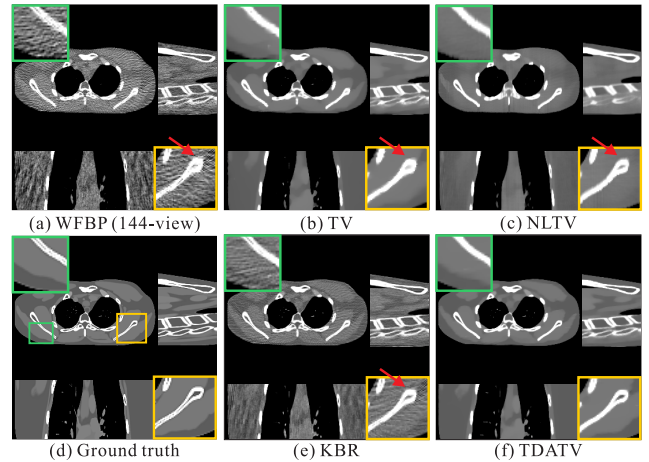

FIGURE 6. Results of the XCAT phantom reconstructed by the WFBP, TV, NLTV, KBR, and TDATV algorithms from 144-view projections. All images are displayed with the same window of [−140, 260] HU.
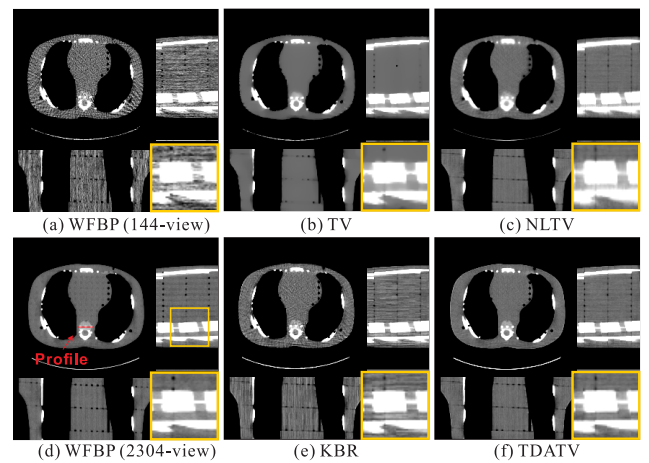

FIGURE 7. Results of the CIRS ATOM phantom reconstructed by the WFBP, TV, NLTV, KBR, and TDATV algorithms from 144-view projections. All images are displayed with the same window of [−140, 260] HU.
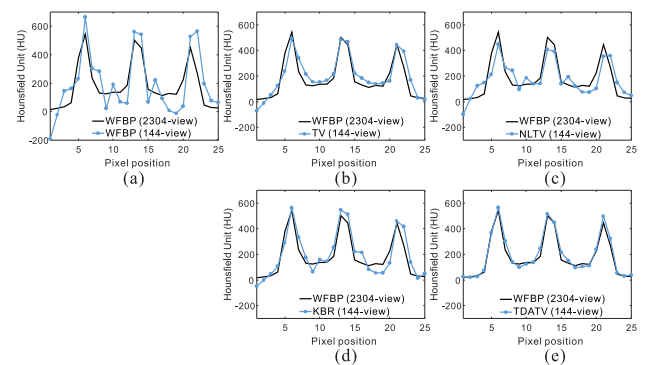

FIGURE 8. Profile comparison between the 2304-view image and different reconstruction methods. From (a) to (e): WFBP (114-view), TV, NLTV, KBR, and the proposed TDATV. The vertical profile is indicated by the red line in Fig. 7 (d).

The KBR algorithm suppresses noise effectively and maintains resolution, but its reconstructed image still contaminated by SHAs (especially streaking artifacts), as shown in the zoom-in ROI of Fig. 6 (e). The TDATV algorithm yields
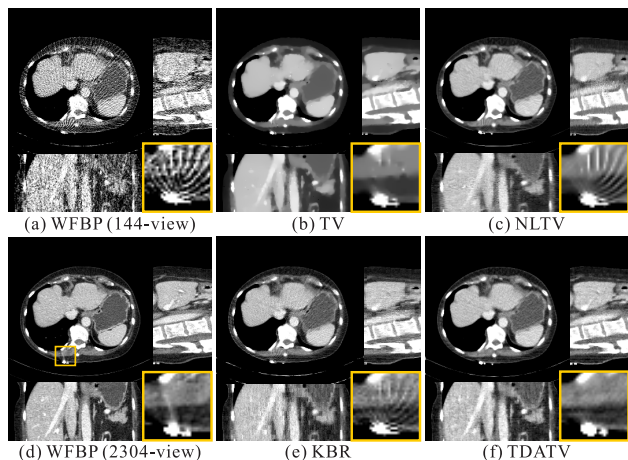
FIGURE 9. Results of patient case 1 reconstructed by the WFBP, TV, NLTV, KBR, and TDATV algorithms from 144-view projections. All images are displayed with the same window of [-140, 260] HU.
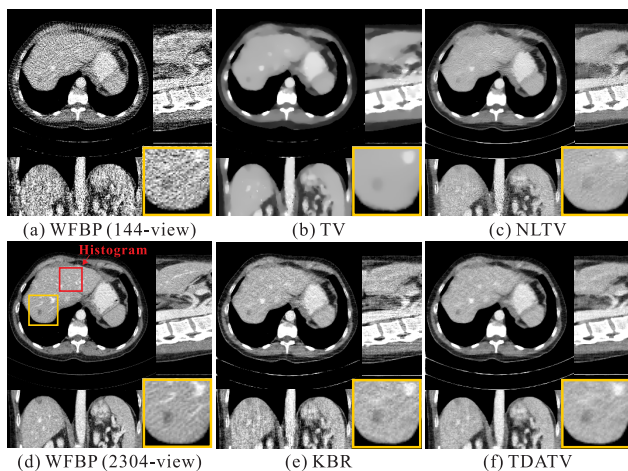

FIGURE 10. Results of patient case 2 reconstructed by the WFBP, TV, NLTV, KBR, and TDATV algorithms from 144-view projections. All images are displayed with the same window of [-140, 260] HU.

the best result in terms of noise and artifact suppression as well as resolution preservation. To quantitatively evaluate the performance of the TDATV algorithm, the PSNR and FSIM of the XCAT phantom results are listed in Table 1 with different algorithms. Compared with the WFBP results of 144- and 288-view, the remaining methods have different degrees of improvement in both PSNR and FSIM. The proposed TDATV achieves the highest performance than all comparison methods.

TABLE 1. Quantitative comparison of the XCAT phantom results (256 × 256 × 100) with different methods.

Views	Indices	WFBP	TV	NLTV	KBR	TDATV
144	PSNR	25.61	30.76	31.38	30.68	**33.02**
	FSIM	0.821	0.956	0.963	0.938	**0.975**
	Time (s)	19.24	123.4	293.4	673.3	842.2
288	PSNR	27.52	34.36	34.76	34.17	**36.08**
	FSIM	0.932	0.973	0.981	0.978	**0.989**
	Time (s)	24.52	153.2	326.1	713.2	896.4

The CIRS ATOM physical phantom was also reconstructed from the real projection data to evaluate the performance of
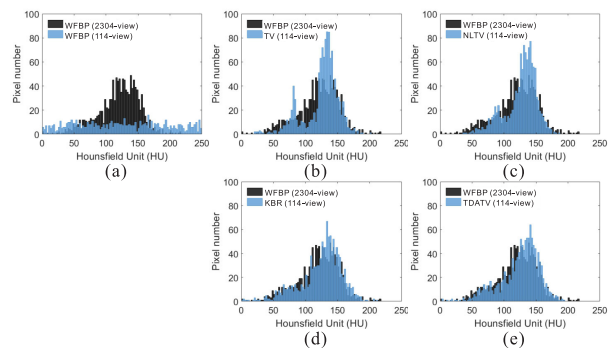

FIGURE 11. Histogram comparison between ROIs of the 2304-view image and images of the five reconstruction methods, from (a) to (e): WFBP (114-view), TV, NLTV, KBR, and the proposed TDATV. The histogram ROI is indicated by the red box in Fig. 10 (d).
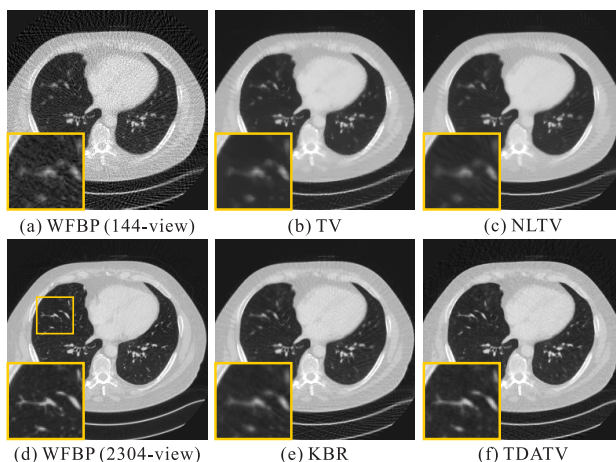

FIGURE 12. Results of patient case 3 reconstructed by the WFBP, TV, NLTV, KBR, and TDATV algorithms from 144-view projections. All images are displayed with the same window of [−1150, 350] HU.

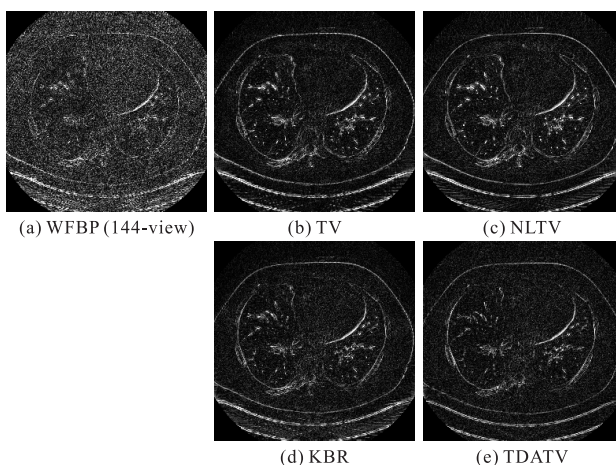FIGURE 13. The absolute residual images of results shown in Fig. 12 with respect to the reference image of 2304-view.

the proposed TDATV, as shown in Fig. 7. The WFBP result of the 2304-view (FFSZ) is considered to be the reference image. The image reconstructed by the TV algorithm loses most of the structural details and the NLTV algorithm is still contaminated by the artifacts. The proposed TDATV method
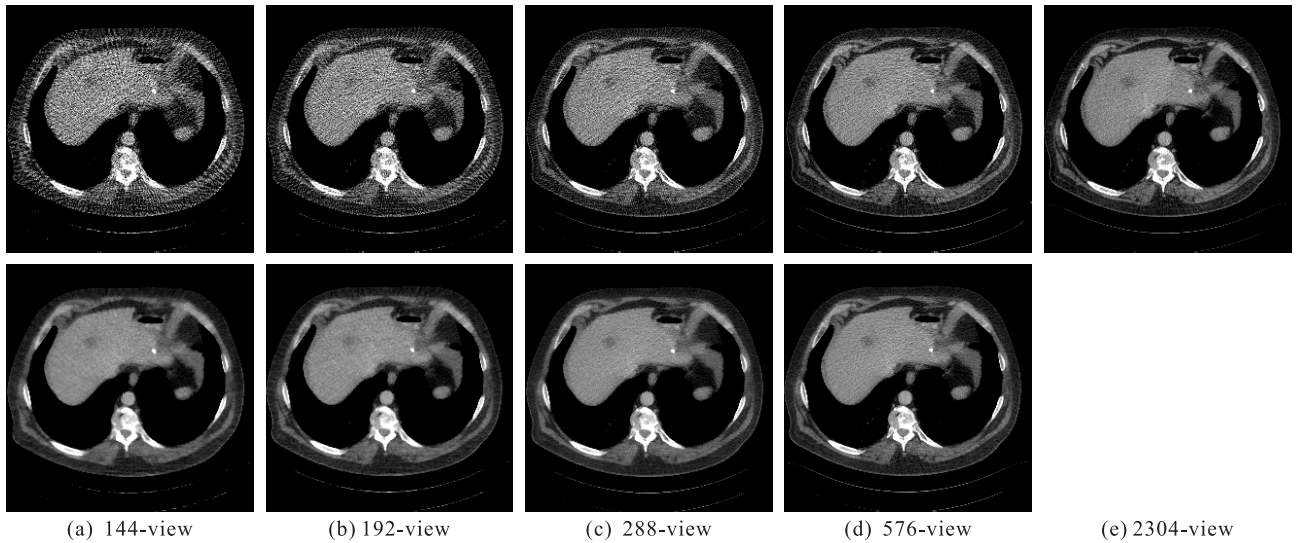
|(a) 144-view|(b) 192-view|(c) 288-view|(d) 576-view|(e) 2304-view|

FIGURE 14. Results of patient case 3 reconstructed with different sparse levels. The top and bottom images are reconstructed with the WFBP and TDATV methods, respectively. All images are displayed with the same window of [-140, 260] HU.

obtains the best result in noise and SHAs reduction, and its result is the closest to the reference image. Fig. 8 depicts the horizontal profiles to illustrate the resolution retention capabilities of the different methods, which are indicated by the red line in Fig. 7 (d). It can be observed that the profile of the TDATV algorithm is closer to the 2304-view result compared to the other comparison reconstruction methods, which illustrates that TDATV maintains better resolution.

B. PATIENT STUDY

Fig. 9 show the results of patient case 1 reconstructed with five different methods from 144-view projections. The WFBP result of the 2304-view (FFSZ) is considered to be the reference image. In the zoom-in ROIs of Fig. 9, it can be observed that in SHCT reconstruction, the high attenuation objects may cause more serious artifacts. Although competing algorithms can remove noise and artifacts to different extents, they are still contaminated by severe artifacts caused by high attenuation objects. By comparison, the proposed TDATV can suppress almost all artifacts.

Fig. 10 shows the results of patient case 2 with hemangioma. It can be seen that the WFBP result is difficult to identify the lesion submerged in severe noise and SHAs. Although the lesion can be identified in different regularization methods, the competing methods lose most liver textures. In contrast, TDATV achieves the desired results in lesion imaging while maintaining more liver texture. Moreover, Fig. 11 shows the ROI histograms of the full-view image, and of images using different reconstruction algorithms. The ROIs are selected from part of the liver of patient case 2, which is indicated by the red box in Fig. 10 (d). It can be observed that the histogram of the TDATV is the closest to that of the full-view image, which further illustrates the superiority of the proposed algorithm.

Fig. 12 shows the results of lung imaging, from which it can be observed that the WFBP image is corrupted with

noise and SHAs. Although competing methods can remove these artifacts, lose most of the details of the lung. In contrast, the TDATV removes noise and SHAs while preserving details of lung. The results demonstrate that TDATV has the best performance in preserving the lung details, as shown in the zoom-in ROIs of Fig. 12. To further validate TDATV, the absolute residuals between the images reconstructed with each competing method and the reference 2304-view image are depicted in Fig. 13. It can be observed that TDATV achieves the smallest residuals relative to other competing methods, which indicates that TDATV preserves the most details while suppressing the most noise and artifacts.

To exploit the influence of sparse levels on the performance of TDATV, experiments were conducted using the patient case 3 with different sparse levels, including 144-, 192-, 288-, and 576-view. Reconstructed images are shown in Fig. 14, where the fine structures are preserved better as the number of views increases and images obtained by TDATV are much better than those of the WFBP. In addition, the PSNR and FISM of results with different sparse levels are computed and ploted in Fig. 15. It can be observed that the PSNR and FISM values obtained by TDATV better than those of the WFBP.

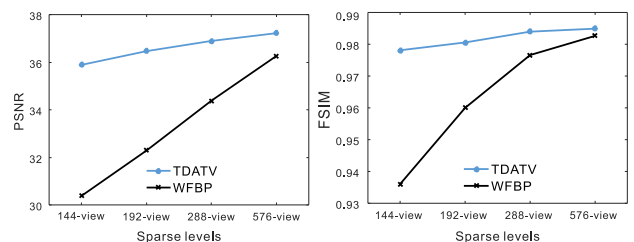

FIGURE 15. Quantitative comparison of reconstructed images with different sparsity levels in patient case 3.

To evaluate the proposed TDATV in the clinical performance, five radiologists with at least three years of

experience in reading CT images were invited to score all the patient images from 0 (worst) to 5 (best) based on noise and artifact reduction, resolution and structure preservation, and lesion detectability [3]. The mean values of the scores from 144-view projections are listed in Table 2. It can be seen that the TDATV obtains the highest scores over all competing methods. The results further demonstrate that the proposed TDATV is superior to other methods through both visual inspection and subjective evaluation.

TABLE 2. Mean of the scores of the patient images reconstructed by 144-view projections.

Patient case	Full-view WFBP	Sparse-view WFBP	TV	NLTV	KBR	TDATV
1	**4.62**	2.94	3.64	3.54	3.44	**4.10**
2	**4.75**	3.16	3.75	3.34	3.32	**3.94**
3	**4.10**	2.82	3.50	3.20	3.54	**3.80**
4	**4.80**	3.10	3.26	3.10	3.42	**3.96**
5	**4.32**	2.80	3.40	3.74	3.74	**4.08**

VI. DISCUSSION AND CONCLUSION

In this work, we study the acquisition protocol of sparse-view helical CT (SHCT) that reduces the radiation dose to ultra-low-dose level. In our experiments, we consider reconstructing the 144-view projections that are 6.25 % of the normal dose (2304-view). However, SHCT reconstructions are contaminated by complex sparse-view helical artifacts (SHAs) that are different from the representations of sparse-view circular artifacts, as shown in Fig. 1. Moreover, normal tissues are also submerged with noises, as shown in Fig. 2.

To address these problems, we propose a tensor decomposition and anisotropic total variation regularization model (TDATV) for SHCT iterative reconstruction. The motivation behind the proposed TDATV is to fully exploit the 3D anatomical structure sparsity in SHCT imaging, including the anatomical structure redundancy and piecewise-smooth, as shown in Fig. 5. The XCAT phantom, CIRS ATOM phantom, and clinical patient studies are employed to validate the performance of the TDATV algorithm. Results demonstrated that the proposed TDATV is superior to all competing methods, including TV, NLTV, and KBR, in both visual assessment and quantitative analysis.

In conclusion, the results demonstrated that SHCT could serve as a potential solution for reducing HCT radiation dose to ultra-low level by using the proposed TDATV model. Nevertheless, the presented work also has potential limitations. First, the quality descriptors PSNR and FSIM are selected for quantitative analysis of SHCT imaging, while they are not well-correlated with the actual diagnostic performance [41]. Therefore, the task-driven image quality assessment, such as multi-case multi-reader study, would be further explored in our future studies. Second, the parameters of the TDATV are tuned in a trial-and-error manner using different types of data, which is time-consuming and suboptimal. How to select the optimal parameters remains an open question for the community. Fortunately, potential techniques, such as deep learning methods, can automatically select

CT reconstruction parameters by learning labeled data [23]. Thus, such methods will be introduced to the proposed TDATV model in future work.

REFERENCES

[1] R. Smithbindman, J. Lipson, R. Marcus, K.-P. Kim, M. Mahesh, R. Gould, A. B. de González, and D. L. Miglioretti, "Radiation dose associated with common computed tomography examinations and the associated lifetime attributable risk of cancer," *Arch. Internal Med.*, vol. 169, no. 22, pp. 2078–2086, 2009.

[2] J. Ma, Z. Liang, Y. Fan, Y. Liu, J. Huang, W. Chen, and H. Lu, "Variance analysis of X-ray CT sinograms in the presence of electronic noise background," *Med. Phys.*, vol. 39, no. 7, pp. 4051–4065, Jun. 2012.

[3] X. Tao, H. Zhang, Y. Wang, G. Yan, D. Zeng, W. Chen, and J. Ma, "VVBP-tensor in the FBP algorithm: Its properties and application in low-dose CT reconstruction," *IEEE Trans. Med. Imag.*, vol. 39, no. 3, pp. 764–776, Mar. 2020.

[4] E. Y. Sidky and X. Pan, "Image reconstruction in circular cone-beam computed tomography by constrained, total-variation minimization," *Phys. Med. Biol.*, vol. 53, no. 17, pp. 4777–4807, Sep. 2008.

[5] S. Niu, Y. Gao, Z. Bian, J. Huang, W. Chen, G. Yu, Z. Liang, and J. Ma, "Sparse-view X-ray CT reconstruction via total generalized variation regularization," *Phys. Med. Biol.*, vol. 59, no. 12, pp. 2997–3017, Jun. 2014.

[6] R. Tovey, M. Benning, C. Brune, M. J. Lagerwerf, S. M. Collins, R. K. Leary, P. A. Midgley, and C.-B. Schönlieb, "Directional sinogram inpainting for limited angle tomography," *Inverse Problems*, vol. 35, no. 2, Feb. 2019, Art. no. 024004.

[7] H. Yu and G. Wang, "Compressed sensing based interior tomography," *Phys. Med. Biol.*, vol. 54, no. 9, pp. 2791–2805, May 2009.

[8] L. L. Geyer, U. J. Schoepf, F. G. Meinel, J. W. Nance, G. Bastarrika, J. A. Leipsic, N. S. Paul, M. Rengo, A. Laghi, and C. N. De Cecco, "State of the art: Iterative CT reconstruction techniques," *Radiology*, vol. 276, no. 2, pp. 339–357, Aug. 2015.

[9] Q. Ding, Y. Long, X. Zhang, and J. A. Fessler, "Statistical image reconstruction using mixed Poisson–Gaussian noise model for X-ray CT," 2018, *arXiv:1801.09533*. [Online]. Available: http://arxiv.org/abs/1801.09533

[10] L. Fu, T.-C. Lee, S. M. Kim, A. M. Alessio, P. E. Kinahan, K. Chang, K. Sauer, M. K. Kalra, and B. De Man, "Comparison between pre-log and post-log statistical models in ultra-low-dose CT reconstruction," *IEEE Trans. Med. Imag.*, vol. 36, no. 3, pp. 707–720, Mar. 2017.

[11] M. G. Wagner, J. L. Hinshaw, Y. Li, T. P. Szczykutowicz, P. Laeseke, C. A. Mistretta, and F. T. Lee, "Ultra–low radiation dose CT fluoroscopy for percutaneous interventions: A porcine feasibility study," *Radiology*, vol. 291, no. 1, pp. 241–249, Apr. 2019.

[12] S. Niu, G. Yu, J. Ma, and J. Wang, "Nonlocal low-rank and sparse matrix decomposition for spectral CT reconstruction," *Inverse Problems*, vol. 34, no. 2, Feb. 2018, Art. no. 024003.

[13] P. Bao, H. Sun, Z. Wang, Y. Zhang, W. Xia, K. Yang, W. Chen, M. Chen, Y. Xi, S. Niu, J. Zhou, and H. Zhang, "Convolutional sparse coding for compressed sensing CT reconstruction," *IEEE Trans. Med. Imag.*, vol. 38, no. 11, pp. 2607–2619, Nov. 2019.

[14] T. G. Flohr, K. Stierstorfer, S. Ulzheimer, H. Bruder, A. N. Primak, and C. H. McCollough, "Image reconstruction and image quality evaluation for a 64-slice CT scanner with z-flying focal spot," *Med. Phys.*, vol. 32, no. 8, pp. 2536–2547, Jul. 2005.

[15] M. Kachelriess, M. Knaup, C. Penssel, and W. A. Kalender, "Flying focal spot (FFS) in cone-beam CT," *IEEE Trans. Nucl. Sci.*, vol. 53, no. 3, pp. 1238–1247, Jun. 2006.

[16] H. K. Tuy, "An inversion formula for cone-beam reconstruction," *SIAM J. Appl. Math.*, vol. 43, no. 3, pp. 546–552, Jun. 1983.

[17] A. Katsevich, "Theoretically exact filtered backprojection-type inversion algorithm for spiral CT," *SIAM J. Appl. Math.*, vol. 62, no. 6, pp. 2012–2026, Jan. 2002.

[18] K. Stierstorfer, A. Rauscher, J. Boese, H. Bruder, S. Schaller, and T. Flohr, "Weighted FBP—A simple approximate 3D FBP algorithm for multislice spiral CT with good dose usage for arbitrary pitch," *Phys. Med. Biol.*, vol. 49, no. 11, pp. 2209–2218, Jun. 2004.

[19] J. Hoffman, S. Young, F. Noo, and M. McNitt-Gray, "Technical note: FreeCT_wFBP: A robust, efficient, open-source implementation of weighted filtered backprojection for helical, fan-beam CT," *Med. Phys.*, vol. 43, no. 3, pp. 1411–1420, Feb. 2016.

[20] S. Schaller, F. Noo, F. Sauer, K. C. Tam, G. Lauritsch, and T. Flohr, "Exact radon rebinning algorithm for the long object problem in helical cone-beam CT," *IEEE Trans. Med. Imag.*, vol. 19, no. 5, pp. 361–375, May 2000.

[21] D. Zeng, Q. Xie, W. Cao, J. Lin, H. Zhang, S. Zhang, J. Huang, Z. Bian, D. Meng, Z. Xu, Z. Liang, W. Chen, and J. Ma, "Low-dose dynamic cerebral perfusion computed tomography reconstruction via Kronecker-basis-representation tensor sparsity regularization," *IEEE Trans. Med. Imag.*, vol. 36, no. 12, pp. 2546–2556, Dec. 2017.

[22] H. Nien and J. A. Fessler, "Fast X-ray CT image reconstruction using a linearized augmented lagrangian method with ordered subsets," *IEEE Trans. Med. Imag.*, vol. 34, no. 2, pp. 388–399, Feb. 2015.

[23] J. He, Y. Yang, Y. Wang, D. Zeng, Z. Bian, H. Zhang, J. Sun, Z. Xu, and J. Ma, "Optimizing a parameterized plug-and-play ADMM for iterative low-dose CT reconstruction," *IEEE Trans. Med. Imag.*, vol. 38, no. 2, pp. 371–382, Feb. 2019.

[24] W. Xu and K. Mueller, "Efficient low-dose CT artifact mitigation using an artifact-matched prior scan," *Med. Phys.*, vol. 39, no. 8, pp. 4748–4760, Jul. 2012.

[25] H. Zhang, D. Zeng, H. Zhang, J. Wang, Z. Liang, and J. Ma, "Applications of nonlocal means algorithm in low-dose X-ray CT image processing and reconstruction: A review," *Med. Phys.*, vol. 44, no. 3, pp. 1168–1185, Mar. 2017.

[26] Y. Zhang, H. Lu, J. Rong, J. Meng, J. Shang, P. Ren, and J. Zhang, "Adaptive non-local means on local principle neighborhood for noise/artifacts reduction in low-dose CT images," *Med. Phys.*, vol. 44, no. 9, pp. e230–e241, Sep. 2017.

[27] Y. Wang, Y. Liao, Y. Zhang, J. He, S. Li, Z. Bian, H. Zhang, Y. Gao, D. Meng, W. Zuo, D. Zeng, and J. Ma, "Iterative quality enhancement via residual-artifact learning networks for low-dose CT," *Phys. Med. Biol.*, vol. 63, no. 21, Oct. 2018, Art. no. 215004.

[28] E. Kang, W. Chang, J. Yoo, and J. C. Ye, "Deep convolutional framelet denosing for low-dose CT via wavelet residual network," *IEEE Trans. Med. Imag.*, vol. 37, no. 6, pp. 1358–1369, Jun. 2018.

[29] H. Chen, Y. Zhang, Y. Chen, J. Zhang, W. Zhang, H. Sun, Y. Lv, P. Liao, J. Zhou, and G. Wang, "LEARN: Learned experts' assessment-based reconstruction network for sparse-data CT," *IEEE Trans. Med. Imag.*, vol. 37, no. 6, pp. 1333–1347, Jun. 2018.

[30] B. Zhu, J. Z. Liu, S. F. Cauley, B. R. Rosen, and M. S. Rosen, "Image reconstruction by domain-transform manifold learning," *Nature*, vol. 555, no. 7697, pp. 487–492, Mar. 2018.

[31] Y. Li, K. Li, C. Zhang, J. Montoya, and G.-H. Chen, "Learning to reconstruct computed tomography images directly from sinogram data under a variety of data acquisition conditions," *IEEE Trans. Med. Imag.*, vol. 38, no. 10, pp. 2469–2481, Oct. 2019.

[32] C. McCollough, "TU-FG-207A-04: Overview of the low dose CT grand challenge," *Med. Phys.*, vol. 43, no. 6, pp. 3759–3760, Jun. 2016.

[33] Q. Xie, Q. Zhao, D. Meng, and Z. Xu, "Kronecker-basis-representation based tensor sparsity and its applications to tensor recovery," *IEEE Trans. Pattern Anal. Mach. Intell.*, vol. 40, no. 8, pp. 1888–1902, Aug. 2018.

[34] W. Wu, F. Liu, Y. Zhang, Q. Wang, and H. Yu, "Non-local low-rank cube-based tensor factorization for spectral CT reconstruction," *IEEE Trans. Med. Imag.*, vol. 38, no. 4, pp. 1079–1093, Apr. 2019.

[35] R. Fang, S. Zhang, T. Chen, and P. C. Sanelli, "Robust low-dose CT perfusion deconvolution via tensor total-variation regularization," *IEEE Trans. Med. Imag.*, vol. 34, no. 7, pp. 1533–1548, Jul. 2015.

[36] W. Dong, G. Shi, Y. Ma, and X. Li, "Image restoration via simultaneous sparse coding: Where structured sparsity meets Gaussian scale mixture," *Int. J. Comput. Vis.*, vol. 114, nos. 2–3, pp. 217–232, Sep. 2015.

[37] L. De Lathauwer, B. De Moor, and J. Vandewalle, "A multilinear singular value decomposition," *SIAM J. Matrix Anal. Appl.*, vol. 21, no. 4, pp. 1253–1278, 2000.

[38] D. Zeng, J. Huang, Z. Bian, S. Niu, H. Zhang, Q. Feng, Z. Liang, and J. Ma, "A simple low-dose X-ray CT simulation from high-dose scan," *IEEE Trans. Nucl. Sci.*, vol. 62, no. 5, pp. 2226–2233, Oct. 2015.

[39] H. Kim, J. Chen, A. Wang, C. Chuang, M. Held, and J. Pouliot, "Non-local total-variation (NLTV) minimization combined with reweighted L1-norm for compressed sensing CT reconstruction," *Phys. Med. Biol.*, vol. 61, no. 18, pp. 6878–6891, Sep. 2016.

[40] L. Zhang, L. Zhang, X. Mou, and D. Zhang, "FSIM: A feature similarity index for image quality assessment," *IEEE Trans. Image Process.*, vol. 20, no. 8, pp. 2378–2386, Aug. 2011.

[41] J. G. Fletcher, L. Yu, J. L. Fidler, D. L. Levin, D. R. DeLone, D. M. Hough, N. Takahashi, S. K. Venkatesh, A.-M. G. Sykes, D. White, R. M. Lindell, A. L. Kotsenas, N. G. Campeau, V. T. Lehman, A. C. Bartley, S. Leng, D. R. Holmes, III, A. Y. Toledano, R. E. Carte, and C. H. McCollough, "Estimation of observer performance for reduced radiation dose levels in CT: Eliminating reduced dose levels that are too low is the first step," *Academic Radiol.*, vol. 24, pp. 876–890, Jul. 2017.

YONGBO WANG received the B.S. degree in biomedical engineering from Southern Medical University, in 2016, China, where he is currently pursuing the Ph.D. degree in biomedical engineering. His research interests include helical CT imaging, and CT image processing theory and methods.

GAOFENG CHEN received the master's degree in biomedical engineering from Southern Medical University, in 2020. His research interest includes CT imaging.

XI TAO received the Ph.D. degree in biomedical engineering from Southern Medical University, China, in 2019. He is currently a Postdoctoral Researcher with the School of Biomedical Engineering, Southern Medical University. His research interests include X-ray medical imaging and machine learning.

ZHAOYING BIAN received the Ph.D. degree in biomedical engineering from Southern Medical University, Guangzhou, China, in 2015. Then, he joined the School of Biomedical Engineering, Southern Medical University. His research interests include CT imaging and PET imaging.

DONG ZENG received the Ph.D. degree in biomedical engineering with Southern Medical University, in 2016. He is currently the Postdoctoral Fellowship with the South China University of Technology. His research interests include low-dose CT imaging and CT image processing theory and methods.

HABIB ZAIDI (Fellow, IEEE) is currently the Chief Physicist and the Head of the PET Instrumentation and Neuroimaging Laboratory, Geneva University Hospital, a Faculty Member with the Medical School, Geneva University, a Professor of medical physics with the University of Groningen, and an Adjunct Professor of molecular imaging with the University of Southern Denmark. He is also actively involved in developing imaging solutions for cutting-edge interdisciplinary biomedical research and clinical diagnosis in addition to lecturing undergraduate and postgraduate courses on medical physics and medical imaging. He was a Guest Editor of 11 special issues of peer-reviewed journals and serves on the Editorial Board of leading journals in *Medical Physics* and *Medical Imaging*. He has been elevated to the grade of Fellow of AIMBE and the AAPM and was elected liaison representative of the International Organization for Medical Physics to the World Health Organization in addition to being affiliated to several international medical physics and nuclear medicine organizations. He is a Developer of physics Web-based instructional modules for the RSNA and an Editor of IPEM's Nuclear Medicine Web-based instructional modules. He received the 2003 Young Investigator Medical Imaging Science Award, the 2004 Mark Tetalman Memorial Award, the 2007 Young Scientist Prize in Biological Physics, the 2010 Kuwait Prize of Applied Sciences, the 2013 John S. Laughlin Young Scientist Award, the 2013 Vikram Sarabhai Oration Award, the 2015 Sir Godfrey Hounsfield Award, the 2017 IBA-Europhysics Prize, and the 2019 Khwarizmi International Award. He has been an invited speaker of more than 160 keynote lectures and talks at an international level and has authored more than 300 peer-reviewed articles in prominent journals and is the Editor of four textbooks.

JI HE received the B.S. and Ph.D. degrees in biomedical engineering from Southern Medical University, China, in 2013 and 2019, respectively. He is currently a Postdoctoral Researcher with the School of Biomedical Engineering, Southern Medical University. His research interests include X-ray medical imaging, machine learning, and deep learning.

JIANHUA MA received the B.S. degree in mathematics from Qufu Normal University, Shandong, China, in 2002, and the Ph.D. degree in biomedical engineering from Southern Medical University, Guangzhou, China, in 2008. He is currently a Professor with the School of Biomedical Engineering, Southern Medical University. His primary research interests in CT imaging include low-dose CT, data correction, image processing, and deep learning. As the Director of the Guangzhou Key Laboratory of Medical Radiation Imaging and Detection Technology, he has been leading multiple NSFC projects in CT imaging.

●●●